Research Article

SOHAG JOURNAL OF SCIENCES

https://doi.org/10.21608/sjsci.2025.395269.1280

Boosting Zinc-Air Battery Stability Using Potassium Ferrocyanide as a Corrosion Inhibitor under CO_2 Exposure

Mostafa Adel*, Mahmoud Elrouby, Abdelrahman Elsayed

[1] Chemistry Department, Faculty of Science, Sohag University, 82524, Sohag, Egypt
*Corresponding emails :Mostafa.adel@science.sohag.edu.eg

Received: 17th June 2025 **Revised:** 17th July 2025 **Accepted:** 29th July 2025
Published online: 10th Septamper 2025

Abstract: This study investigates the enhancement of electrochemical performance and corrosion resistance of zinc (Zn) electrodes in zinc–air batteries using 5 M KOH electrolyte modified with potassium ferrocyanide as an inorganic corrosion inhibitor. The impact of CO_2 exposure on the inhibition efficiency and electrode stability was also evaluated. The addition of 0.02 M potassium ferrocyanide reduced the corrosion current density and achieved an inhibition efficiency of 42.32% at 25 °C. Notably, the combined presence of CO_2 and ferrocyanide further increased the inhibition efficiency to 76.72%, demonstrating a strong combined effect. Electrochemical impedance spectroscopy revealed a maximum charge transfer resistance of 137.39 Ω·cm² in the CO_2 + ferrocyanide system, indicating effective surface passivation. These results were supported by Tafel analysis and surface characterization techniques (SEM, EDS, XRD), which confirmed the formation of a protective mixed corrosion product layer. Overall, the combined use of potassium ferrocyanide and CO_2 significantly enhances the corrosion resistance, discharge capacity, and electrochemical stability of Zn electrodes, offering a promising strategy to improve the performance and lifespan of alkaline zinc–air batteries.
Keywords: Zinc-battery; inorganic inhibitor; Tafel Polarization; Carbon dioxide; Charge-discharge

1. Introduction

Zinc is a widely used anode material in the production of alkaline batteries due to its high theoretical energy density, low cost, environmental friendliness, and safety profile [1]. However, in alkaline electrolytes, zinc is highly susceptible to corrosion, which significantly impairs battery performance by reducing capacity, cyclability, and shelf life [2]. In recent years, advanced zinc-based batteries have been developed for various energy storage applications [3]. Among them, primary systems such as Zn–air, Zn–MnO_2, Zn–carbon, and Zn–Ag batteries have effectively utilized metallic zinc as an anode, leveraging its high energy density, ease of reversibility, and sustainable nature [4]. Despite these advantages, zinc anodes still suffer from major operational challenges—including dendritic growth and hydrogen evolution reactions (HER)—during the discharge process. Nevertheless, the inherent reversibility of zinc electrochemistry in aqueous systems continues to make it a highly attractive material for secondary battery technologies [5-7]. As a result, numerous studies addressed these flaws. First, a variety of elements, including Mg, Ga, In, Mn, Sn, Ti, and Zr, were alloyed with zinc. These elements' alloying with zinc resulted in a strong hydrogen overpotential [8, 9]. Additionally, dendritic formation and zinc shape distortion were considerably decreased by a minor alloying of In, Bi, and Ni with zinc [10-12]. Thus, the capacity of the zinc electrode serving as an anode in simple batteries is increased by alloying the aforementioned components with zinc. Electrolyte additions were applied to the zinc surface to improve corrosion resistance and significantly slow down the evolution of hydrogen gas. This led to an improvement in discharge performance [13]. In alkaline battery systems, zinc electrode corrosion was inhibited by a few organic inhibitors, including di-nonylphenol phosphate ester, polyethylene glycol (600), tartrate, and α-diphenyl-1-glyoxime [14]. They stated that the adsorption of organic species on the investigated zinc metal surface happened as a result of the addition of organic additives to the electrolyte. Qu et al. [15] demonstrated that the desorption kinetics were quick following the citation of the battery potential and anodic process at rest, suggesting that the zinc surface is coated with an efficient inhibitor molecule. This conduct, however, has a detrimental effect on zinc's discharge performance and ought to be avoided. Several other organic substances, including benzotriazole, thiourea, and sodium dodecyl benzene sulfonate, were investigated as zinc corrosion inhibitors [16]. According to the results, benzotriazole exhibits greater inhibitory activity than the other chemicals described. Huang et al. [17] investigated how the electrochemical behaviour of zinc electrodes, that is utilized in zinc-air batteries, was affected by the addition of certain organic chemicals, including polysorbate 20, EDTA, and tartaric acid. It has been noted that EDTA exhibits powerful inhibitory behaviour in lowering corrosion processes and stopping dendritic development. However, little research has been done on how inorganic chemicals in the alkaline electrolyte [18, 19] affect the corrosion of the metal in question (zinc) and its alloys [20-28]. With increasing potassium ferrocyanide addition, the development of corrosion resistance, suppression of developed hydrogen, cycle lifespan, and discharge capacity were demonstrated and contrasted with those without it. Furthermore, corrosion is reduced more effectively when CO_2 is present than when it is not. In this study, various electrochemical techniques, including Tafel polarization, electrochemical impedance

spectroscopy (EIS), and galvanostatic charge–discharge testing, were used to evaluate the corrosion behavior and energy performance of zinc electrodes in alkaline media with and without CO_2. The surface composition and morphology of the corrosion products were characterized using scanning electron microscopy (SEM), elemental mapping, and X-ray diffraction (XRD). This work aims to provide new insights into effective corrosion inhibition strategies for enhancing the durability and efficiency of zinc-based anodes in advanced alkaline battery systems.

2. Experimental Section

2.1. Chemicals and Materials

A 5 M KOH solution was prepared by dissolving an appropriate amount of analytical-grade potassium hydroxide (BDH) in bidistilled water. Using the same procedure, potassium ferrocyanide ($K_4[Fe(CN)_6]$) was introduced into the electrolyte at varying concentrations of 0.005 M, 0.01 M, 0.015 M, and 0.02 M. Although $K_4[Fe(CN)_6]$ is commonly employed in alkaline media, its solubility is limited by the common ion effect in the presence of KOH [29]. To counteract this limitation, a saturated CO_2 solution was generated by continuously bubbling pure CO_2 gas into the 5 M KOH electrolyte for approximately five hours at a controlled flow rate. The gas was supplied from a pressurized CO_2 cylinder, and the saturation process was monitored by measuring the solution's pH until it stabilized around 9. For electrode fabrication, high-purity zinc metal (99.99%, Johnson Matthey Chemicals Ltd.) was used to produce disc-shaped zinc electrodes (surface area = 0.5028 cm^2). The zinc was sealed in an evacuated silicon tube and subjected to heating at 750 °C for 24 hours to achieve complete fusion. During this period, the molten metal was agitated every three hours to promote homogeneity. The fused zinc was then rapidly quenched by immersion in an ice bath to solidify the electrode.

2.2. Characterization

The crystalline phases of the fabricated electrode were identified using a high-precision X-ray diffractometer (Bruker AXS D8) with Cu-Kα radiation (λ = 1.5418 Å). The surface morphology and elemental composition of the working electrode were examined using energy-dispersive X-ray spectroscopy (EDS) integrated with a scanning electron microscope (SEM, model JSM-IT200).

2.3. Electrochemical Experiments

All electrochemical measurements were conducted using a three-electrode Pyrex glass cell connected to a VersaSTAT4 potentiostat/galvanostat. The working electrode consisted of a zinc disc (exposed area = 0.5028 cm^2), insulated with Teflon and mounted securely in an Araldite holder. Prior to each experiment, the electrode surface was mechanically polished using emery papers with progressively finer grit sizes (800 to 1200 µm), then thoroughly cleaned in pure acetone and rinsed with running bidistilled water.

A platinum sheet served as the counter electrode, while a saturated Ag/AgCl (KCl sat.) electrode was used as the reference for all potential measurements. For electrochemical cleaning, the zinc electrode was immersed in a 5 M KOH solution and polarized at –2 V vs. Ag/AgCl for five minutes. Afterward, the electrode was removed and gently agitated to dislodge any hydrogen bubbles that had formed on the surface.

Subsequent measurements included galvanostatic charge-discharge cycling, Tafel polarization, and electrochemical impedance spectroscopy (EIS) to evaluate the electrode's electrochemical behavior under various test conditions.

2.3.1. Tafel technique

Tafel plots were recorded at various temperatures (25, 35, 45 and 50 °C) over a potential range of –0.25 V to +0.25 V relative to the open-circuit potential (Ecorr), using a scan rate of approximately 0.001 $V \cdot s^{-1}$.

2.3.2. EIS technique

Electrochemical impedance spectroscopy (EIS) measurements were performed using a DC bias of ±100 mV, with an AC perturbation amplitude of 10 mV, over a frequency range spanning from 10 kHz to 1 Hz.

2.3.3. Charge-discharge measurements

Charge–discharge measurements were conducted at a constant current density of ±2 $mA \cdot cm^{-2}$ and a temperature of 25 °C, with a voltage cutoff set at 0 V.

2.4. Assessing the corrosion parameters

At the open-circuit potential (E_{corr}), the working electrode was allowed to reach equilibrium for 30 minutes in a 5 M KOH solution. The corrosion current densities (i_{corr}) were accurately determined by extrapolating the linear portions of the anodic and cathodic Tafel branches to their intersection point. For all measurements, freshly prepared electrolyte solutions and thoroughly cleaned electrodes were used to ensure consistency. The experiments were conducted at three different temperatures-25, 35, 45 and 50°C-using a CW3-10P Heating Bath Circulator, which offers efficient internal and external circulation. Each test was repeated at least three times to ensure high reproducibility, and all electrochemical procedures were consistently repeated under identical conditions.

3. Results and Discussion: -

Electrochemical behaviour of zinc in KOH having different concentrations of Potassium Ferrocyanide

3.1. Tafel plot

Figure 1(a) displays the polarization curves of the zinc electrode in 5 M KOH solution, recorded at a scan rate of 1 $mV \cdot s^{-1}$, both in the absence and presence of varying concentrations of potassium ferrocyanide (0.005,0.01, 0.015, and 0.02 M). The corresponding corrosion parameters were derived by analyzing the Tafel regions of the anodic and cathodic branches (potential vs. current density) and are summarized in **Table 1** [30]. Corrosion current densities (i_{corr}) were determined by extrapolating the linear portions of the Tafel plots to the corrosion potential (E_{corr}). These calculations were performed for the zinc electrode in both the uninhibited and ferrocyanide-containing electrolytes.

As observed, the addition of ferrocyanide causes a pronounced

shift in the polarization curves toward lower i_{corr} values. Increasing the concentration of the inorganic inhibitor results in a marked reduction in corrosion current. Specifically, in pure 5 M KOH, the i_{corr} of zinc was 141.254 µA/cm². This value steadily decreased to 81.47 µA/cm² upon the addition of 0.02 M ferrocyanide at 25 °C, clearly demonstrating the effective corrosion inhibition capability of ferrocyanide in alkaline conditions.

The inhibition efficiency (η%) was calculated using equation (1):

$$\eta\% = \frac{i_p - i_w}{i_p} \times 100 \qquad (1)$$

where i_p and i_w represent the corrosion current densities in uninhibited and inhibited solutions, respectively. An increase in ferrocyanide concentration corresponded with higher η%, indicating enhanced protective behavior. This improvement is attributed to the formation and adherence of zinc oxide layers on the surface, acting as a barrier to corrosion. The surface coverage (θ = η% / 100) followed the same trend, further supporting the interaction between ferrocyanide ions and zinc atoms, possibly promoted by oxygen evolution during the reaction.

Additionally, a slight positive shift in E_{corr} was observed with increasing inhibitor concentration (as shown in Table 1), indicating enhanced thermodynamic stability of the zinc surface. The average corrosion rate (U_{corr}, in mm/year) was estimated using the equation (2):

$$U_{corr.}\left(\frac{mm}{y}\right) = \frac{3270 \times M \times i_{corr.}}{d} \qquad (2)$$

where M is the equivalent weight of zinc (g/equiv), d is the material's density (g/cm³), icorr is the corrosion current density (µA/cm²), and 3270 is a unit-dependent constant. A consistent decline in Ucorr values with higher ferrocyanide concentrations confirmed the inhibitor's effectiveness.

Figure 1(b) further compares the corrosion behavior in the presence and absence of CO_2. Notably, i_{corr} values decreased significantly with CO_2 exposure from 141.254 to 37.41 µA/cm² in the absence of ferrocyanide, and further to 32.88 µA/cm² when 0.02 M ferrocyanide was present. The corresponding E_{corr} values shifted from more negative (–1.55 V without CO_2 and –1.56 V with ferrocyanide) to less negative values (–1.295 V and –1.299 V, respectively), signifying improved corrosion resistance.

Furthermore, the inhibition efficiency rose markedly under CO_2-saturated conditions, reaching 73.52% without ferrocyanide and 76.72% with it. Interestingly, these findings contrast with prior studies in acidic and neutral CO_2-containing media, where CO_2 was reported to enhance corrosion [31]. In this case, however, CO_2 appears to contribute positively to the protection of zinc in an alkaline environment, potentially due to altered surface chemistry or the formation of more adherent protective films.

Overall, these results highlight a promising enhancement in the electrochemical stability and efficiency of zinc electrodes in alkaline battery systems. The reduced corrosion rate directly implies a higher effective utilization of zinc as the anode material, thereby improving the discharge capacity, which is a critical parameter for the performance of zinc–air and other alkaline batteries [32].

The surface morphology and composition of the corrosion products formed on the pure zinc anode in 5 M KOH, with and without 0.02 M potassium ferrocyanide at 25 °C, were investigated using SEM, EDX, and XRD techniques. As illustrated in Figure 2(a, b), the SEM micrographs of the zinc surface after exposure to 5 M KOH without any inhibitor reveal a thick, porous, and irregularly distributed corrosion layer covering nearly the entire electrode surface. The corrosion product particles display non-uniform shapes and sizes, suggesting uncontrolled nucleation and growth, which is characteristic of zinc hydroxide ($Zn(OH)_2$) formation. These observations are consistent with the XRD pattern shown in Figure 3(a), which confirms $Zn(OH)_2$ as the primary corrosion product in the uninhibited electrolyte.

In contrast, the zinc surface treated in the presence of 0.02 M potassium ferrocyanide, shown in Figure 2(c, d), exhibits a noticeably different morphology. The corrosion layer appears finer, more compact, and more uniformly distributed, with smaller particles that are firmly attached to the underlying surface. This change in morphology implies the formation of a more protective and adherent corrosion film. The corresponding XRD pattern in Figure 3(b) indicates the presence of both $Zn(OH)_2$ and ZnO phases. The formation of ZnO, along with slight shifts in the diffraction peaks, suggests that ferrocyanide ions influence the electrochemical reaction pathway and may be incorporated into or adsorbed onto the corrosion layer, modifying its structure and crystallinity.

EDX analysis further supports these findings. As shown in Figure 2(e, f) and summarized in Table 2, the zinc surface corroded in the absence of the inhibitor displays a higher oxygen content and a weaker zinc signal, indicating the presence of a thick $Zn(OH)_2$ layer. In contrast, the sample exposed to ferrocyanide exhibits reduced oxygen content and a more prominent zinc signal, consistent with a thinner, denser, and more protective corrosion film. Minor traces of iron and nitrogen in the inhibited sample may be attributed to the adsorption or incorporation of ferrocyanide species onto the zinc surface.

These morphological and compositional results align well with the electrochemical data, which showed a significant reduction in corrosion current density (icorr) in the presence of ferrocyanide. The inhibitor clearly mitigates the formation of extensive $Zn(OH)_2$ layers and promotes the development of a mixed oxide/hydroxide layer with improved surface coverage and integrity. Collectively, these findings confirm that potassium ferrocyanide acts as an effective inorganic corrosion inhibitor for zinc in alkaline media, enhancing surface protection and reducing metal dissolution.

The influence of CO_2 saturation and potassium ferrocyanide addition on the corrosion behavior of zinc in 5 M KOH was examined using SEM mapping, EDX spectroscopy, and XRD analysis, as illustrated in Figure 4 and supported by Figure 3(c,

d). The SEM mapping image in Figure 4(a), representing the zinc surface exposed to 5 M KOH saturated with CO_2 (without ferrocyanide), reveals that the entire electrode surface is coated with a thick, porous, and loosely adherent corrosion layer. The observed particle morphology is heterogeneous, indicating the formation of mixed corrosion products. This is corroborated by the XRD patterns in Figure 3(c), which confirm the presence of

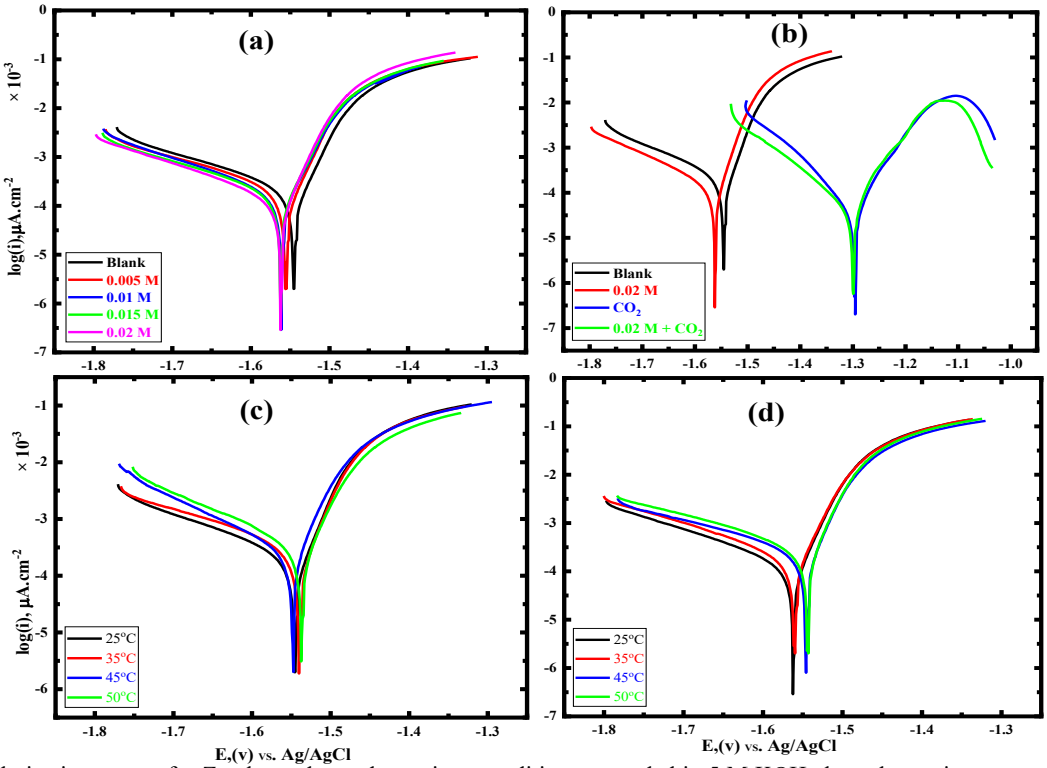

Figure 1. Tafel polarization curves for Zn electrodes under various conditions, recorded in 5 M KOH electrolyte using a scan rate of 0.01 V·s^{-1}: (a) In the absence of CO_2, with different concentrations of ferrocyanide ions (0–0.02 M) at 25 °C; (b) In the absence and presence of CO_2, with and without 0.02 M ferrocyanide at 25 °C; (c) At different temperatures (25, 35, 45, and 50 °C) in 5 M KOH without ferrocyanide; (d) At the same temperatures in 5 M KOH containing 0.02 M ferrocyanide.

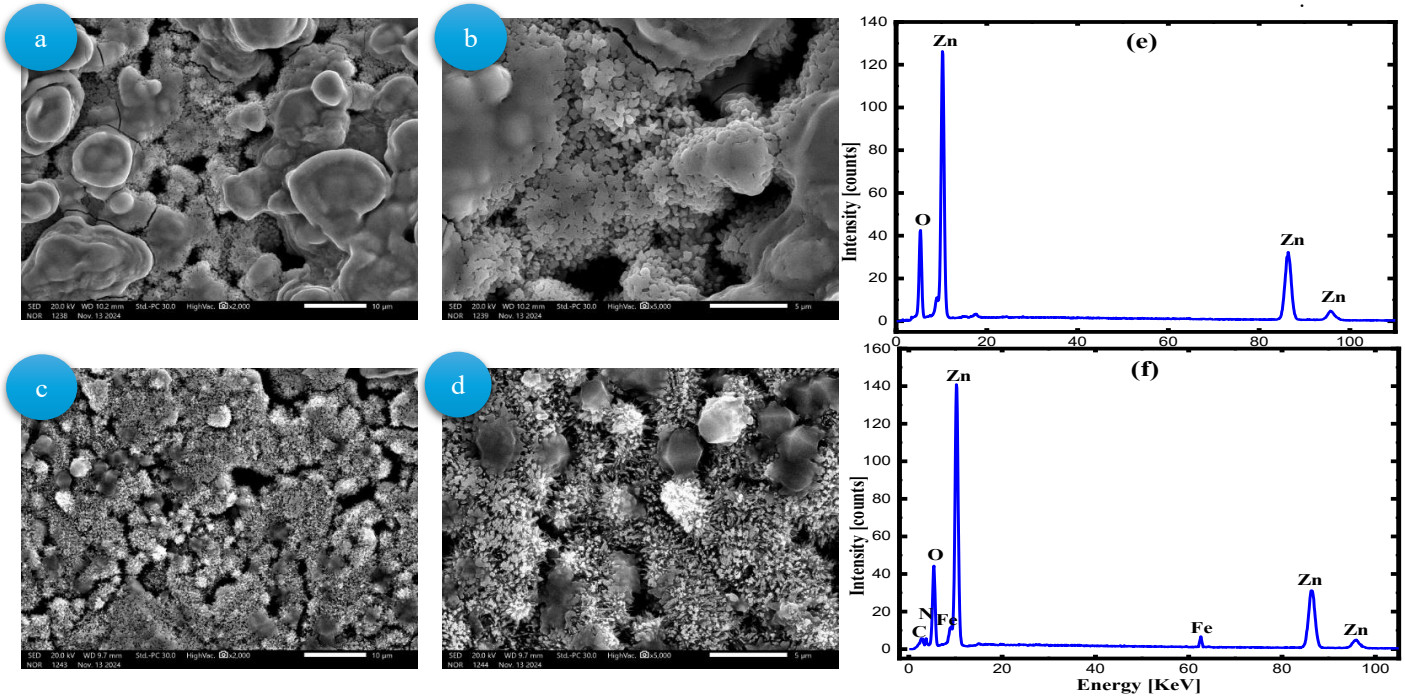

Figure 2. Images taken using SEM at 2,000 and 5,000 magnification, and also EDX analysis charts of the oxide layer for Zn electrode (a, b, e) in 5 M KOH without and with Ferrocyanide ions (c, d, f) at 25 °C, respectively, at the active region.

newly formed zinc carbonate ($ZnCO_3$) and zinc carbonate hydroxide, both of which are absent in the system without CO_2. The generation of $ZnCO_3$-related species implies that CO_2 reacts with zinc ions and hydroxide in the alkaline electrolyte to form insoluble surface films that act as barriers, inhibiting the direct formation of $Zn(OH)_2$ and ZnO.

The formation of these carbonate-based phases slows down the dissolution process of zinc, thus mitigating corrosion. It can be inferred that in a CO_2-saturated environment, the development of $ZnCO_3$ limits the availability of free zinc ions to form $Zn(OH)_2$ or ZnO, thereby decreasing the corrosion rate and enhancing surface passivation.

In comparison, **Figure 4(b)** shows the SEM mapping of the zinc electrode in the presence of both CO_2 and 0.02 M potassium ferrocyanide. The corrosion products in this case appear finer, more compact, and more uniformly distributed, with particles showing tighter adhesion to the substrate. This structural refinement indicates that ferrocyanide ions further enhance surface protection, possibly by adsorbing onto the zinc surface, modifying the nucleation and growth of corrosion products, and suppressing hydrogen evolution reactions.

The XRD spectrum in **Figure 3(d)** confirms the co-presence of $Zn(OH)_2$, ZnO, and $ZnCO_3$. The existence of ZnO alongside $ZnCO_3$ suggests partial oxidation pathways are still active, but the rate is significantly reduced due to the combined influence of ferrocyanide and carbonate film formation. Moreover, the shift in diffraction peak positions hints at structural modifications likely caused by ferrocyanide adsorption and incorporation into the surface layer.

The EDX spectra and mapping shown in **Figure 4(c, d)**, along with elemental composition data in Table 3, reinforce these interpretations. In the CO_2-only environment (**Figure 4c**), the oxygen and carbon signals are dominant, consistent with a carbonate-rich layer. However, in the CO_2 + ferrocyanide system (**Figure 4d**), the presence of nitrogen and iron signals confirms the adsorption of ferrocyanide ions. Additionally, the zinc and oxygen signals indicate a thinner and more controlled corrosion product layer, further supporting the inhibitory effect of the additive. From an electrochemical standpoint, these observations align with previously obtained Tafel and EIS data, which demonstrated a substantial decrease in corrosion current density (i_{corr}) in the presence of CO_2, and an even greater reduction when ferrocyanide was added, reaching a maximum inhibition efficiency of 76.72%. This confirms that the synergistic action of CO_2 and potassium ferrocyanide results in a more protective surface layer, effectively retarding zinc dissolution and improving the electrode's long-term stability.

In conclusion, the SEM, XRD, and EDX results collectively indicate that the electrolyte system containing 5 M KOH saturated with CO_2 and supplemented with potassium ferrocyanide offers enhanced corrosion resistance by promoting the formation of insoluble protective layers ($ZnCO_3$, ZnO, $Zn(OH)_2$) and facilitating inhibitor adsorption. These findings suggest that this electrolyte formulation is a promising candidate for improving the longevity and performance of zinc anodes in alkaline battery systems.

Effect of Temperature

To better understand the adsorption behavior of ferrocyanide ions on the zinc electrode surface and their effect on corrosion inhibition, potentiodynamic polarization studies were carried out in 5 M KOH containing the maximum ferrocyanide concentration (0.02 M) at different electrolyte temperatures (25, 35, 45, and 50 °C), as shown in Figure 1(c, d). The corrosion parameters indicate that increasing the solution temperature results in a positive shift in the corrosion potential (Ecorr) and a corresponding increase in the corrosion current density (icorr). These observations suggest that both the anodic dissolution of zinc and the hydrogen evolution reaction intensify with rising temperature [33]. A closer look at the cathodic branches of the Tafel plots shows a modest increase in current density over the 25–50 °C range, indicating a slight enhancement in hydrogen evolution kinetics. However, the relatively small changes imply that the cathodic process is not strongly temperature-dependent within this range [34]. The presence of ferrocyanide ions appears to increase the hydrogen overpotential, thereby delaying hydrogen gas evolution. As a result, higher potentials are required for hydrogen formation at elevated temperatures, indicating stronger inhibition by ferrocyanide under these conditions.

The electrochemical parameters obtained at each temperature are summarized in Table 1. Minor changes in the anodic and cathodic Tafel slopes (β_a and β_c) with increasing temperature suggest that while the corrosion rate increases, the underlying electrochemical mechanisms remain unchanged. Rather, the temperature rise seems to activate additional reactive surface sites without altering the reaction pathway.

Moreover, the results show that surface coverage and inhibition efficiency improve with increasing temperature, even at a fixed ferrocyanide concentration. This enhancement supports the hypothesis that ferrocyanide ions adsorb more effectively at elevated temperatures, thereby providing better surface protection and slowing the corrosion process [35]. Such behavior is characteristic of physisorption, further confirming the slight interaction between ferrocyanide ions and the zinc surface.

The Arrhenius plots for the zinc electrode in the presence and absence of ferrocyanide, presented in Figure 5(a), were used to estimate the activation energy of the corrosion process. The relationship follows the Arrhenius equation (3), which describes how temperature affects the corrosion rate and allows for quantifying the energy barrier associated with the electrochemical reaction.

$$\ln i_{\text{corr.}} = \frac{-E_a}{RT} + \ln A \qquad (3)$$

In this context, Ea represents the activation energy ($kJ \cdot mol^{-1}$), R is the universal gas constant ($J \cdot mol^{-1} \cdot K^{-1}$), A denotes the pre-exponential factor, and T is the absolute temperature in Kelvin. The calculated activation energy values for the zinc electrode in the investigated electrolyte, both in the absence and presence of 0.02 M ferrocyanide, are presented in Table 4. The results show that the presence of the inhibitor leads to a noticeable increase in Ea, indicating that ferrocyanide ions effectively raise the energy barrier for the corrosion process. This enhancement

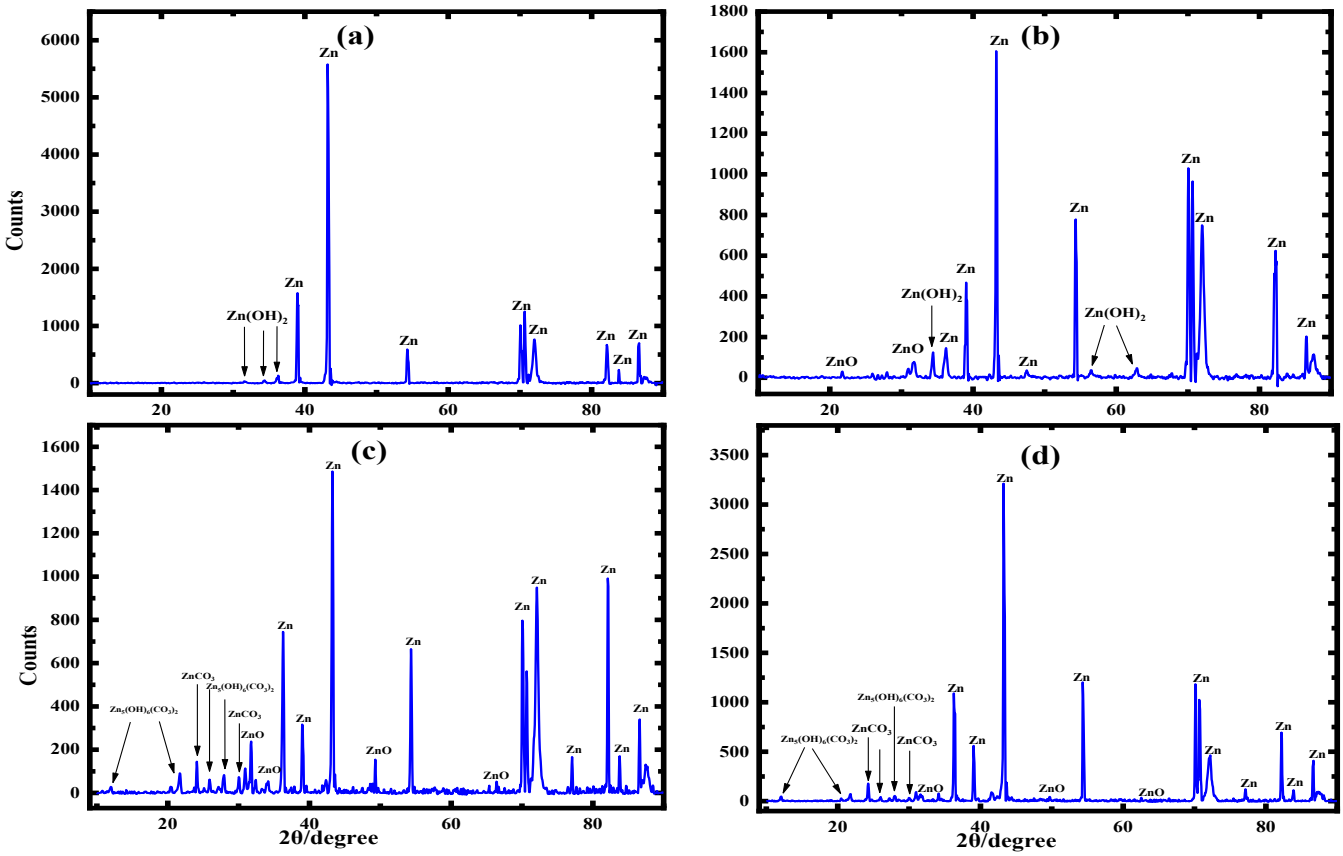

Figure 3. XRD Patterns of the electrochemical products formed on the surfaces of Zinc electrode in 5 M KOH without and with Ferrocyanide ions when CO_2 is present (a, b) and when it is absent (c, d) at 25°C in the active region, respectively.

Table 1. Corrosion parameters for zinc were determined from Tafel polarization in 5 M KOH with and without Ferrocyanide ions in the absence and presence of CO_2 at different temperatures.

Electrolytes	Parameters						
	$i_{corr.}$ (μA / cm^2)	- $E_{corr.}$ (V vs. Ag/AgCl)	β_a(mV/ decade)	- βc (mV/ decade)	Ucorr. (mm/y)	η%	θ
25°C							
Blank	141.254	1.544	36.48	112.72	2.115	-	-
0.005 M	119.62	1.554	29.34	108.73	1.791	15.32	0.153
0.01 M	106.17	1.561	25.93	110.36	1.589	24.84	0.248
0.015 M	92.257	1.562	34.2	111.85	1.381	34.68	0.346
0.02 M	81.47	1.562	26.6	127.45	1.219	42.32	0.423
CO_2	37.41	1.295	49.74	79.14	0.560	73.52	0.735
0.02 M +CO_2	32.88	1.299	44.1	92.69	0.492	76.72	0.767
35°C							
Blank	163.31	1.540	34.24	121.5	2.445	-	-
0.02 M	96.64	1.559	33.69	123.7	1.447	40.82	0.408
45°C							
Blank	189.67	1.547	32.62	151.37	2.840	-	-
0.02 M	118.21	1.545	31.53	101.61	1.770	37.67	0.376
50°C							
Blank	204.37	1.537	30.34	166.34	3.06	-	-
0.02 M	129.45	1.543	29.48	115.73	1.938	36.65	0.366

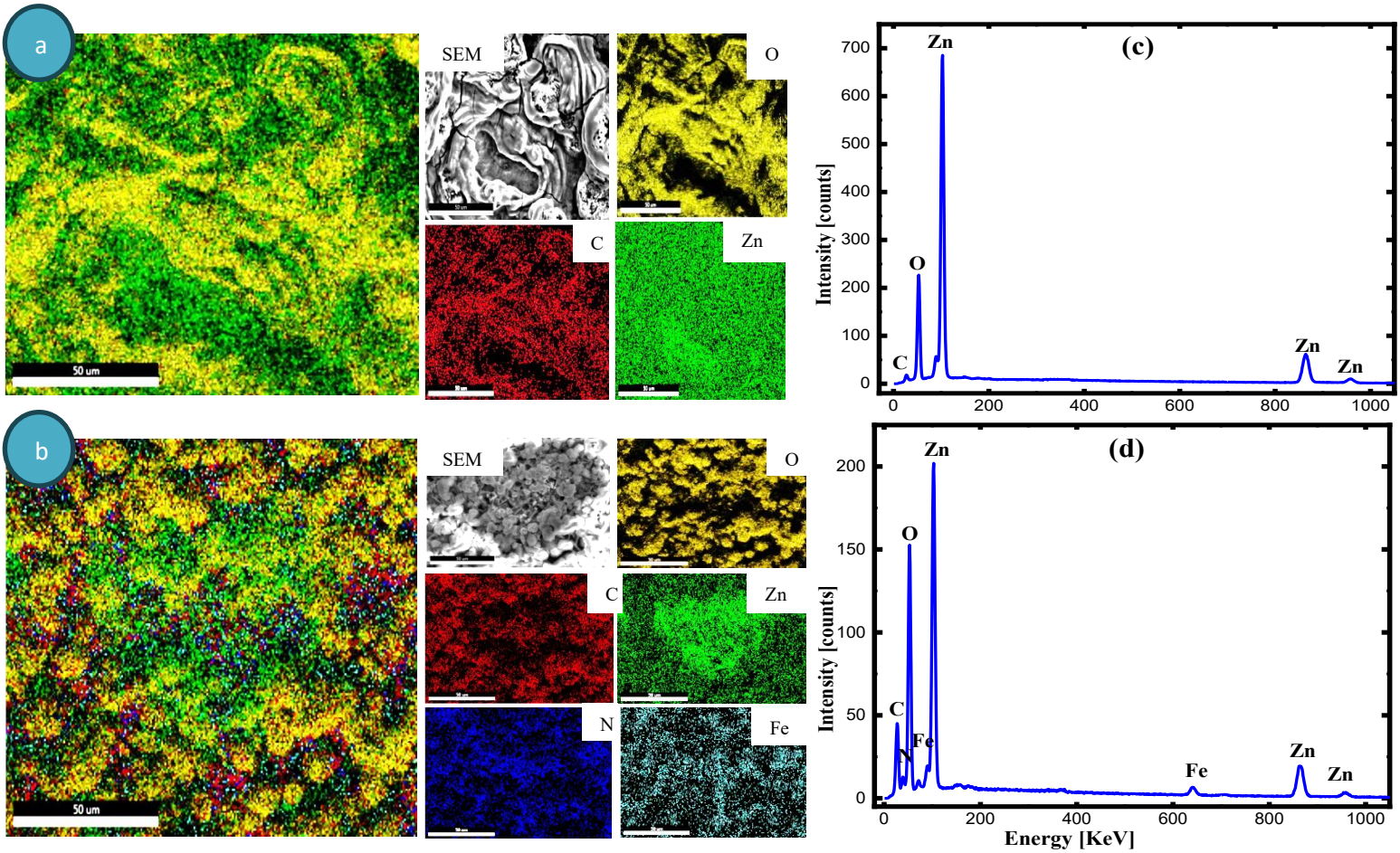

Figure 4. Elemental mapping, Scanning electron microscopy (SEM) Images (a, b) at 2,000 magnification of the oxide layer for Zn electrode and energy dispersive X-ray spectroscopy (EDS) spectra (c, d) in 5 M KOH without ferrocyanide ions and with Ferrocyanide ions in the presence of CO_2 at 25°C, respectively, at the active region.

Table 2. EDS data for zinc in 5 M KOH without and with Ferrocyanide ions.

Electrolyte	Element	Line	Mass%	Atom%
5 M KOH	O	K	21.15±0.13	52.28±0.32
	Zn	K	78.85±0.46	47.72±0.28
	Total		100.00	100.00
5 M KOH + 0.02 M	C	K	7.37±0.09	19.91±0.24
	N	K	0.22±0.04	0.50±0.09
	O	K	21.97±0.13	44.59±0.27
	Fe	K	0.17±0.02	0.10±0.01
	Zn	K	70.27±0.41	34.90±0.21
	Total		100.00	100.00

Table 3. EDS data for zinc in 5 M KOH without and with Ferrocyanide ions in the presence of CO_2.

Electrolyte	Element	Line	Mass%	Atom%
5 M KOH + CO_2	C	K	10.9	28.0
	O	K	20.4	39.5
	Zn	K	68.7	32.5
	Total		100.00	100.00
5 M KOH + CO_2 + 0.02 M	C	K	30.5	49.8
	N	K	3.9	5.5
	O	K	27.0	33.0
	Fe	K	2.2	0.8
	Zn	K	36.3	10.9
	Total		100.00	100.00

suggests that the ferrocyanide species form a strongly adsorbed protective layer on the zinc surface, which hinders the electrochemical dissolution of the electrode and thus slows down the corrosion rate [36].

To understand the mechanisms of electrochemical processes, it is essential to examine and interpret adsorption isotherms. The surface coverage (θ) at varying inhibitor concentrations can be estimated from potentiodynamic polarization data using the relation θ = η% / 100 [37]. The selection of an appropriate adsorption model depends on several factors, including the chemical interaction between the inhibitor and the electrode surface, the adsorption equilibrium constant (K_{ads}), and the extent of surface coverage. The mode of ferrocyanide ions adsorption during the corrosion inhibition process reflects the nature of the interaction between the inhibitor and the corroding zinc surface [38]. Analyzing the adsorption behavior provides valuable insight into how the additive interacts with the electrode interface.

To quantify this behavior, the relationship between θ and the inhibitor concentration (C_{inh}) was tested against various isotherm models, including Frumkin, Temkin, Freundlich–Huggins, and Langmuir models. Among these, the Langmuir adsorption isotherm provided the best fit, indicating uniform adsorption sites and monolayer adsorption behavior, with no significant interaction between adsorbed species [39]. The Langmuir model assumes that every adsorption site is equivalent and independent of neighboring site occupancy. The linearized form of the Langmuir isotherm is expressed by equation (4):

$$\frac{C_{inh.}}{\theta} = C_{inh.} + \frac{1}{K_{ads.}} \qquad (4)$$

where C_{inh} represents the ferrocyanide ion concentration and K_{ads} represents the adsorption equilibrium constant for the process. The electrode surface's adsorption. As seen by the straight lines of the $C_{inh.}$ / θ vs. Cinh graphs Fiq.5 (b), the adsorption on the electrode surface conformed to the Langmuir adsorption model.

The regression coefficient for the fitted curve is roughly equivalent to one (R^2 = 0.937). The tendency to inhibit is caused by the layer's adsorption on the electrode surface. The best simulation for the Langmuir adsorption isotherm is shown by the $C_{inh.}$ / θ against C_{inh} plots, which have slopes that are nearly equal to one (slope = 0.935). The K_{ads} value was calculated using the intercept of the straight line on the $C_{inh.}$ /θ axis [40], where it equals 34.27. The following equation (5) was then used to relate it to the standard Gibbs free energy ΔG^o_{ads} [41].

$$K_{ads} = \frac{1}{55.5} e^{\left(-\frac{\Delta G^o_{ads}}{RT}\right)} \qquad (5)$$

The electrolyte under examination has a water molar content of 55.5 mol L^{-1}. The higher adsorption of Ferrocyanide ions is the cause of the high value of K_{ads} for the zinc electrode and is brought about by the homogeneity of the surface-active sites under investigation. [42]. Additionally, higher inhibitory effectiveness and more efficient adsorption are indicated by larger K_{ads} values [43]. It's important to observe that the ΔG_{ads} value is -18.71 kJ mol^{-1}, which indicates that physisorption [44] plays a role in the examined additives' adsorption on the tested electrode surface [45]. Additionally, the efficiency of the inhibitive activity increases as ferrocyanide ions accumulation increases Table 1.

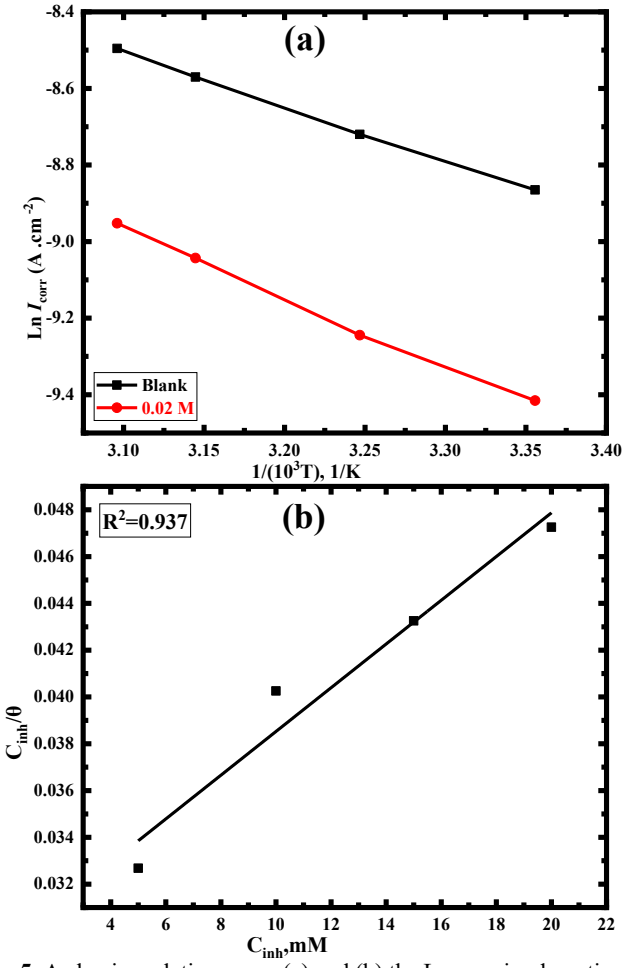

Figure 5. Arrhenius relation curve (a) and (b) the Langmuir adsorption model ($C_{inh.}$/θ vs. $C_{inh.}$) fitting data derived from Tafel polarization measurements for the Zn electrode in the investigated alkaline electrolyte with varying $K_4[Fe(CN)_6]$ concentrations at 25 ◦C.

Table 2. The electrochemical corrosion reaction's E_a values for the zinc electrode in 5 M KOH without and with Ferrocyanide ions.

Electrolyte	$E_{a.}$ (KJ/mole)
Blank	11.823
0.02 M	14.943

3.2. EIS measurements

The results of potentiodynamic polarization investigations have been verified by the EIS of the zinc anode in the alkaline electrolyte with different ferrocyanide ion concentrations. It has been studied how potassium ferrocyanide (0.005, 0.01, 0.015, and 0.02 M) inhibits zinc metal. EIS is well recognized as an effective method for studying electrode kinetics, surface properties, and the corrosion process. Mechanistic information is provided by impedance diagrams [46]. Nyquist plots for the investigated electrode in the studied alkaline solution with and

without ferrocyanide ions present in varying concentrations are shown in Figure 6(a). A suitable semicircle is chosen to simulate the impedance data at $E_{corr.}$. According to the data, the high-frequency component of the impedance response of the electrodes under investigation shows a loop of compressed semicircular, while the low-frequency portion shows a straight line. The diffusion of zincate ions from the anode's surface to the electrolyte's bulk is most likely what causes the straight line (Z_w) that is seen in the low-frequency region, while the resistance of charge transfer ($R_{ct.}$) is linked to the semicircular loop at a higher frequency. This low-frequency tail represents the Warburg impedance, which reflects diffusion-controlled mass transport processes of electroactive species, particularly zincate ions, through the electrolyte. Therefore, the Warburg element provides insight into the limitations of ionic diffusion and its influence on the overall electrochemical behavior. The properties of the investigated electrode in the aforementioned scenario can be described by the analogous circuit shown in Figure 7 (a). One way to characterize this behaviour is that the electron transfer resistance associated with the influence of the ionic double-layer capacitance is the primary source of the semicircle (at high frequencies). Both the double layer's capacity (C_{dl}) and the resistance of charge transfer (R_{ct}) are calculated using the Bode plot of the impedance spectrum. The computed data indicate that when ferrocyanide ions are added to the specified electrolyte, the charge transfer resistance increases while the C_{dl} values decrease. Depending on the C_{dl} values, either the thickness of the electrical double layer has increased, or the local dielectric constant has reduced. This illustrates how the inhibitor ions work by adhering to surfaces at the solution/interface [47]. Conversely, as C_{dl} values decrease as the additive concentration rises, the inhibitor is probably going to cover a larger surface area, which will increase the inhibition's efficacy. About 1.1 and 1.2 ohms is the solution resistance R_s for zinc, which is essentially constant. Furthermore, the concentration of ferrocyanide ions in the solution is observed to increase with the Warburg impedance. Because ferrocyanide ions have a greater covered surface area and strong adsorption, this shows that protection rises with increasing additive concentrations. Conversely, it is noted that the addition of ferrocyanide ions to the alkaline electrolyte does not affect the impedance profile. This indicates that both the pure alkaline solution and the addition of ferrocyanide ions exhibit comparable dissolving mechanisms for the metal under investigation. Increased zinc's R_{ct} values frequently signify corrosion inhibition, which lowers electrochemical polarization [48]. As previously stated, the debate concludes that the growing influx of ferrocyanide ions to the electrolyte has caused inhibitors to be adsorbed on the surface and form layers on the zinc anode. Higher R_{ct} values and lower C_{dl} values are consistent with the ferrocyanide layer thickness growing as the concentration of ferrocyanide ions in the solution rose. This is because the exposed surface area and the double-layer capacitance are directly correlated. The thicker the layer of ferrocyanide ions on the electrode substrate compared to the pure medium, the greater the barrier to charge transfer. This could suggest that the resulting ferrocyanide film is more impervious to the entrance of (OH^-) ions, hence enhancing the surface layer's resistance to corrosion. The results showed that the surface layer's protection against corrosive media had been strengthened. These findings demonstrated the thicker ferrocyanide layer's reduced solubility, which resulted in anti-corrosion properties [49].

Analysis of zinc's electrochemical impedance spectroscopy in an alkaline electrolyte with different potassium ferrocyanide concentrations, both with and without carbon dioxide. The Nyquist graphs for zinc in the investigated alkaline solution with different ferrocyanide ion concentrations (0.005, 0.01, 0.015, and 0.02 M) measured at (10 mV) AC magnitude are shown in Fig.6 (a). The frequencies, at 25 ◦C, vary from 10^4 Hz to 1 Hz. Figure 6 (b) shows the Bode plot of impedance modulus against frequency, and Figure 6 (c) shows the phase angle against frequency for the zinc electrode in the solution. The Bode plot was used to drive the parameters, which were mentioned in Table 5, and include the resistance of charge transfer (R_{ct}), the resistance of polarization (R_p), the resistance of solution (R_s), and the double layer C_{dl} capacitance. Fig. 7(a) shows the analogous circuit that is recommended for fitting the obtained impedance parameters. The absence of CO_2 results in a flattened semicircle with a tiny diffusion tail at low-frequency values of all impedance spectra. This indicates that Warburg impedance is caused by the dissolved zincate ions moving from the surface of the electrode under examination to the inner solution. In contrast, the resistance of charge transfer ($R_{ct.}$) is linked to the semicircular loop at a greater frequency. It is important to note that the impedance behaviour profile is unaffected by the fluctuation that occurs when ferrocyanide ions are added, suggesting a similar mechanism for preventing Zn electrode corrosion [50]. The impedance at high frequencies is commonly used to indicate the surface coating response, giving details about that specific film. As previously stated, the XRD results showed that this film is made up of ZnO and $Zn(OH)_2$ when ferrocyanide ions are present, and $Zn(OH)_2$ only when they are not. Low frequencies are thus used to reveal the chemical process at the substrate/solution contact [51]. The values of R_{ct} and Z_w increase as the concentration of ferrocyanide ions rises, as shown by the recorded data in Table 5 [52]. The electric double layer capacity C_{dl} without and with an additive, respectively, is represented by the following equivalent circuit (Fig. 7a). The practical Nyquist semi-circuit yielded values that were consistent with the evaluated values from the equivalent circuit. This shows that ferrocyanide ions have increased the surface coverage of the electrode under study, indicating that surface coatings are effective at postponing processes of corrosion [53]. This demonstrates that ferrocyanide ions lower the evaluated electrode's electrical capacity by dislodging H_2O molecules and OH^- ions, which were mostly produced on the surface under investigation. R_{ct} values rise as a result. Additionally, as the concentration of ferrocyanide ions increases, values of C_{dl} exhibit a declining tendency. This suggests that this phenomenon is caused by a decrease in the dielectric double layer. This behaviour supports the physisorption mechanism of ferrocyanide ions at the metal/solution contact [54]. Between 1.1 Ω and 1.2 Ω, the solution resistance Rs is nearly constant. The double-layer capacitance (C_{dl}) can be calculated using the following equation.

$$f\left(-Z''_{max}\right) = \frac{1}{2\pi C_{dl} R_{ct}} \qquad (6)$$

Here (- $Z^{//}_{max}$) is the maximal imaginary component of the impedance [55]. According to the potentiodynamic investigation, it can be stated that this process inhibits the evolution of hydrogen and zinc dissolution. This shows that

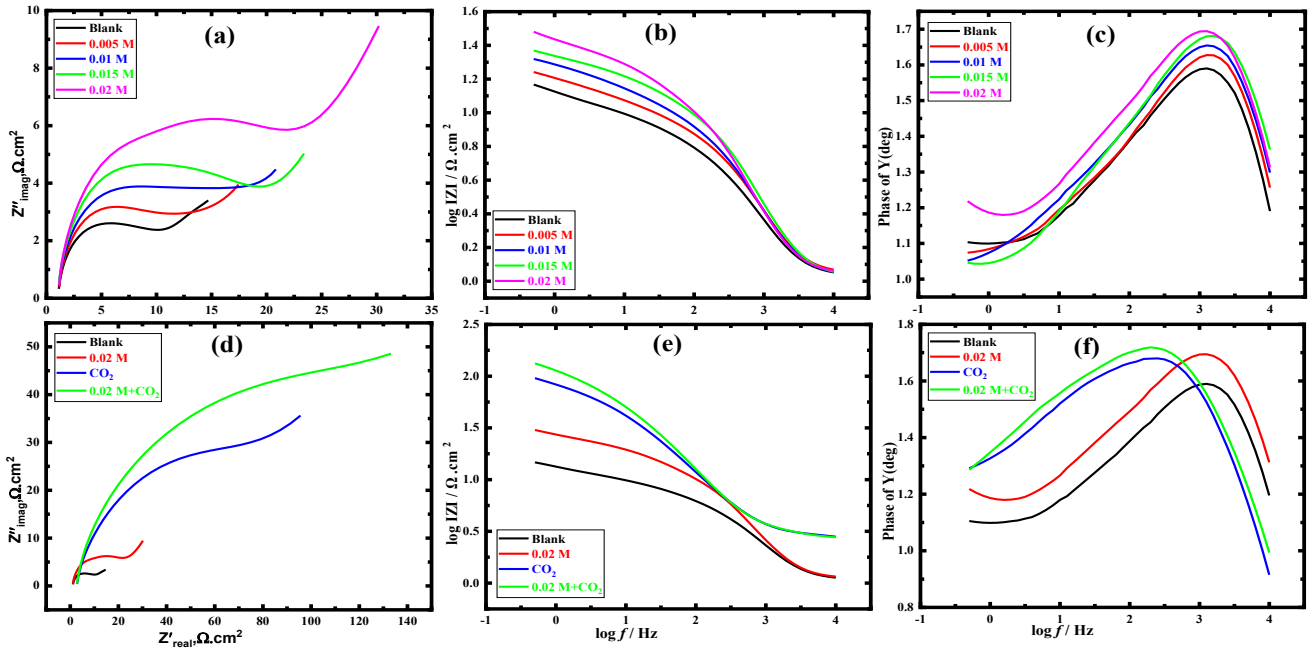

Figure 6. Nyquist plots (a, d), Bode plots (b, e), and phase (c, f) of the Zn electrode in 5 M KOH without and with ferrocyanide ions in the absence and presence of CO_2, respectively, were achieved at 25 °C with frequencies ranging from 10^4 Hz to 1 Hz, vs. OCP, and a magnitude of 10 mV for the Ac voltage.

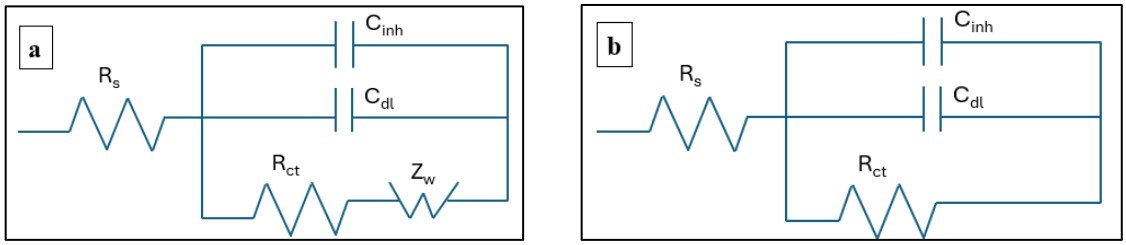

Figure 7. Equivalent circuits for the zinc electrode in the absence and presence of CO_2 (a, b), respectively.

Table 3. EIS parameters for Zn electrode in 5 M KOH without and with ferrocyanide ions in the presence and absence of CO_2 at 25 °C.

Electrolytes	Parameters				
	R_s ($\Omega.cm^2$)	R_p ($\Omega.cm^2$)	R_{ct} ($\Omega.cm^2$)	D (cm^2/s)	C_{dl} ($F.cm^2$)
Blank	1.164	15.134	13.97	4.17×10^{-10}	3.60×10^{-4}
0.005 M	1.229	17.939	16.71	3.48×10^{-10}	3.01×10^{-4}
0.01 M	1.197	21.418	20.221	2.49×10^{-10}	2.49×10^{-4}
0.015 M	1.23	24.021	22.791	2.24×10^{-10}	2.21×10^{-4}
0.02 M	1.223	31.461	30.238	9.56×10^{-11}	1.66×10^{-4}
CO_2	2.855	99.909	97.054	-	5.18×10^{-5}
0.02 M + CO_2	2.814	140.204	137.39	-	3.66×10^{-5}

Ferrocyanide ions adsorption caused a layer of Zn ferrocyanide to develop on the surface under investigation. Zinc deposited from zincate ions is thus inhibited when the investigated additive is present in the electrolyte [56]. One can find the Warburg impedance (Z_w) using the following formula [57].

$$Z' = \sigma \frac{1}{\omega^{1/2}} - j\frac{\sigma}{\omega^{\frac{1}{2}}} \qquad (7)$$

$$|Z'| = \frac{\sqrt{2}\sigma}{\omega^{\frac{1}{2}}} \qquad (8)$$

After evaluating the Warburg plot, the Warburg coefficient (σ) can be found by calculating its slope, the diffusion coefficient is D, which can be calculated as follows [58]:

$$D = \left(\frac{RT}{\sqrt{2}An^2F^2C\sigma}\right)^2 \qquad (9)$$

Where R is the ideal gas constant in J/mol K, T is the temperature in kelvin, A is the electrode surface area in cm^2, n is the number of electrons transferred, F is the Faraday constant in C/mol, and C is the concentration in mol/cm^3. It found that by increasing the concentration of the inhibitor the diffusion coefficient values decrease (see table 5) so it is indication for impedance varburg to increase .

This trend, which points to the beginning of the corrosive processes, is compatible with the polarization section of the Tafel according to the earlier data. Because of this, zinc Nyquist plots show semicircle behaviour at the active region, indicating kinetic control of the electrochemical reaction. This illustrates even more how these results are consistent with Tafel's graph findings. Interestingly, Fig. 6 (d), demonstrates that carbon dioxide is present in the KOH electrolyte, showing that the radius of the semi-circle is much larger for zinc than when CO_2 does not exist, demonstrating how much the solution containing CO_2 resists corrosion. The charge transfer values (R_{ct}) for Zn are 97.054 and 137.39 $\Omega.cm^2$ without and with ferrocyanide ions, respectively. These findings support the Tafel polarization findings. In Figure 6 (e, f), the Bode plot and the phase angle for zinc are displayed when CO_2 is present. Fig. 7(b) shows the analogous circuit that is recommended for fitting the obtained impedance parameters.

3.3. Charge-discharge technique

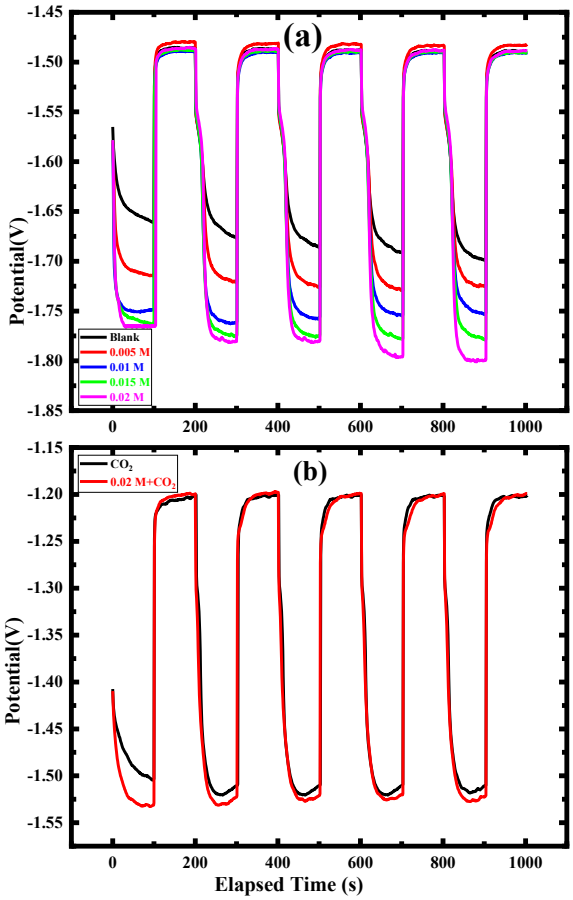

Figure 8. Galvanostatic curves of charge-discharge for zinc electrode in 5 M KOH with different concentrations of ferrocyanide ions in the absence of CO_2 (a) and with 0.02 M ferrocyanide ions in the presence of carbon dioxide (b) at an applied current density of ±2 mA/cm^2 at 25 °C.

Figure 8(a) presents the galvanostatic charge-discharge curves of the zinc electrode in 5 M KOH containing varying concentrations of ferrocyanide inhibitor, tested at a constant current density of ±2 mA· cm^2 at 25 °C. As shown in the figure, increasing the ferrocyanide concentration leads to a noticeable increase in the potential difference during charge-discharge cycles. This indicates enhanced electrochemical behavior and confirms that the zinc electrode exhibits improved charge-

discharge characteristics with higher inhibitor concentrations, resulting in more stable and prolonged discharge performance.

Figure 8(b) shows the charge-discharge profiles of the zinc electrode in 5 M KOH, both with and without the addition of ferrocyanide, in the presence of CO_2 under the same current density conditions. The presence of CO_2 significantly increases both the potential difference and the discharge time compared to the CO_2-free system. This suggests that CO_2 contributes to improved electrode performance, and when combined with ferrocyanide, results in further enhancement, as evidenced by the extended discharge period and greater potential variation. It is well established that the energy density of rechargeable Zn–air batteries is largely influenced by the electrochemical efficiency of the zinc anode in alkaline electrolytes [55].

One of the primary limitations of such systems is the spontaneous evolution of hydrogen gas on the zinc surface, which can interfere with the oxidation of zinc and reduce battery efficiency. The addition of potassium ferrocyanide as an inhibitor helps mitigate this issue by suppressing self-discharge reactions and stabilizing the zinc surface. This leads to improved discharge behavior and overall energy performance of the electrode in alkaline environments.

4. Conclusions

This study demonstrated that incorporating potassium ferrocyanide into a 5 M KOH electrolyte significantly improved the corrosion resistance and electrochemical performance of zinc electrodes. The inhibitor reduced both anodic and cathodic reactions, as confirmed by Tafel and EIS analyses, with increased charge transfer resistance and decreased double-layer capacitance, indicating effective surface adsorption. CO_2 addition further enhanced inhibition efficiency by promoting the formation of a $ZnCO_3$-rich passive film, leading to improved surface protection and discharge behavior. The synergistic effect of ferrocyanide and CO_2 resulted in higher electrochemical stability and capacity, highlighting their potential for enhancing the lifespan and efficiency of alkaline zinc-based batteries. However, due consideration must be given to the long-term stability and environmental risks of ferrocyanide, particularly its potential decomposition under oxidative or photolytic conditions. Future research should address these challenges to support safe and scalable deployment.

Credit authorship contribution statement:

Author Contributions: Conceptualization, Abdelrahman and Mahmoud; methodology, Mostafa; software, Mostafa.; validation, Abdelrahman, Mahmoud and Mostafa; formal analysis, Mahmoud.; investigation, Abdelrahman; resources, Mostafa; data curation, Mahmoud; writing—original draft preparation, Mostafa; writing—review and editing, X.X.; visualization, Abdelrahman; supervision, Mahmoud and Abdelrahman; funding acquisition, Mahmoud, All authors have read and agreed to the published version of the manuscript.

Data availability statement

The data used to support the findings of this study are available from the corresponding author upon request.

Declaration of competing interest

The authors declare that they have no known competing financial interests or personal relationships that could have appeared to influence the work reported in this paper.

References

1. Lei, L., et al., *Strategies to enhance corrosion resistance of Zn electrodes for next generation batteries.* Frontiers in Materials, 2020. **7**: p. 96.
2. Fan, X., et al., *Porous nanocomposite gel polymer electrolyte with high ionic conductivity and superior electrolyte retention capability for long-cycle-life flexible zinc–air batteries.* Nano Energy, 2019. **56**: p. 454-462.
3. Fan, X., et al., *Advances in the development of power supplies for the internet of everything.* InfoMat, 2019. **1**(2): p. 130-139.
4. Chao, D., et al., *An electrolytic Zn–MnO2 battery for high-voltage and scalable energy storage.* Angewandte Chemie, 2019. **131**(23): p. 7905-7910.
5. Amiinu, I.S., et al., *Multifunctional Mo–N/C@ MoS2 electrocatalysts for HER, OER, ORR, and Zn–air batteries.* Advanced Functional Materials, 2017. **27**(44): p. 1702300.
6. Liu, K., et al., *Recent advances in metal–nitrogen–carbon catalysts for electrochemical water splitting.* Materials Chemistry Frontiers, 2017. **1**(11): p. 2155-2173.
7. Zhao, Z., et al., *Challenges in zinc electrodes for alkaline zinc–air batteries: obstacles to commercialization.* ACS Energy Letters, 2019. **4**(9): p. 2259-2270.
8. Zeng, R.-c., et al., *Corrosion resistance of cerium-doped zinc calcium phosphate chemical conversion coatings on AZ31 magnesium alloy.* Transactions of Nonferrous Metals Society of China, 2016. **26**(2): p. 472-483.
9. Bahmani, A., S. Arthanari, and K.S. Shin, *Corrosion behavior of Mg–Mn–Ca alloy: Influences of Al, Sn and Zn.* Journal of Magnesium Alloys, 2019. **7**(1): p. 38-46.
10. Jo, Y.N., et al., *The effects of mechanical alloying on the self-discharge and corrosion behavior in Zn-air batteries.* Journal of industrial engineering chemistry, 2017. **53**: p. 247-252.
11. El-Sayed, A.-R., H.S. Mohran, and H.M. Abd El-Lateef, *Effect of minor nickel alloying with zinc on the electrochemical and corrosion behavior of zinc in alkaline solution.* Journal of Power Sources, 2010. **195**(19): p. 6924-6936.
12. Elrouby, M., H.A.E.S. Shilkamy, and A. Elsayed, *Development of the electrochemical performance of zinc via alloying with indium as anode for alkaline batteries application.* Journal of Alloys Compounds, 2021. **854**: p. 157285.
13. Yang, H., et al., *Improved discharge capacity and suppressed surface passivation of zinc anode in dilute alkaline solution using surfactant additives.* Journal of Power Sources, 2004. **128**(1): p. 97-101.
14. Moon, K.-M., et al., *The effect of additives on the corrosion resistance of Zn electrode in alkaline battery system.* Metals Materials International 2005. **11**: p. 221-226.

15. Qu, D., *Behavior of Dinonylphenol Phosphate Ester and its influence on the oxidation of a Zn anode in alkaline solution.* Journal of power sources, 2006. **162**(1): p. 706-712.
16. Xiao, Y., et al., *Effects of electrolyte additives on the properties of zinc-bismuth electrodes in zinc-air batteries.* Journal of The Electrochemical Society, 2018. **165**(2): p. A47.
17. Huang, M.C., et al., *Improved electrochemical performance of Zn–air secondary batteries via novel organic additives.* Journal of the Chinese Chemical Society, 2018. **65**(10): p. 1239-1244.
18. Zhang, C., et al., *Study of the performance of secondary alkaline pasted zinc electrodes.* Journal of applied electrochemistry, 2001. **31**: p. 1049-1054.
19. El-Sayed, A.-R., H.S. Mohran, and H.M. Abd El-Lateef, *Inhibitive action of ferricyanide complex anion on both corrosion and passivation of zinc and zinc–nickel alloy in the alkaline solution.* Journal of Power Sources, 2011. **196**(15): p. 6573-6582.
20. Ma, J., et al., *Effects of polystyrene sulfonate/graphene and Mn3O4/graphene on property of aluminum (zinc)-air batteries.* International Journal of Hydrogen Energy, 2020. **45**(23): p. 13025-13034.
21. Wang, M., et al., *Defects-rich graphene/carbon quantum dot composites as highly efficient electrocatalysts for aqueous zinc/air batteries.* International Journal of Hydrogen Energy, 2017. **42**(33): p. 21305-21310.
22. Pan, H., et al., *Amino functionalized carbon nanotubes supported CoNi@ CoO–NiO core/shell nanoparticles as highly efficient bifunctional catalyst for rechargeable Zn-air batteries.* International Journal of Hydrogen Energy, 2021. **46**(1): p. 374-388.
23. Costa, J.M., et al., *In-situ transformation of electrodeposited W–Co oxide to ZnCo2O4 nanoparticles as an effective bifunctional catalysts in Zn-air batteries.* International Journal of Hydrogen Energy, 2020. **45**(32): p. 16122-16132.
24. Yin, M., et al., *HNRNPA2B1 as a trigger of RNA switch modulates the miRNA-mediated regulation of CDK6.* Iscience, 2021. **24**(11).
25. Zhang, S., et al., *Anticorrosion of hydrophobic membrane on aluminum electrode for alkaline quasi solid Al-air batteries.* Journal of Power Sources, 2022. **545**: p. 231907.
26. Huang, H., et al., *Novel proton exchange membrane with long-range acid–base-pair proton transfer pathways based on functionalized polyethyleneimine.* ACS Sustainable Chemistry Engineering, 2021. **9**(10): p. 3963-3974.
27. Wei, M., et al., *A Prussian-blue bifunctional interface membrane for enhanced flexible Al–air batteries.* Advanced Functional Materials, 2023. **33**(37): p. 2302243.
28. Wei, M., et al., *A fluoropolymer bifunctional solid membrane interface for improving the discharge duration in aqueous Al–air batteries.* Chemical Communications, 2023. **59**(74): p. 11121-11124.
29. Wang, G., et al., *Unlocking the solubility limit of ferrocyanide for high energy density redox flow batteries.* Materials Today Energy, 2022. **28**: p. 101061.
30. Tremont, R., et al., *3-Mercaptopropyltrimethoxysilane as a Cu corrosion inhibitor in KCl solution.* Journal of Applied Electrochemistry, 2000. **30**: p. 737-743.
31. LeBozec, N., et al., *Atmospheric corrosion of zinc-aluminum alloyed coated steel in depleted carbon dioxide environments.* Journal of The Electrochemical Society, 2018. **165**(7): p. C343.
32. Ren, J., et al., *Electrochemical performance of pure Al, Al–Sn, Al–Mg and Al–Mg–Sn anodes for Al-air batteries.* Journal of Alloys, 2019. **808**: p. 151708.
33. Aouine, Y., et al., *Temperature and time investigations on the adsorption behavior of isoindoline, tetrazole and isoindoline-tetrazole on corrosion of mild steel in acidic medium.* International Journal of Electrochemical Science, 2012. **7**(6): p. 5400-5419.
34. Lee, C.W., et al., *Novel alloys to improve the electrochemical behavior of zinc anodes for zinc/air battery.* Journal of power sources, 2006. **160**(2): p. 1436-1441.
35. El-Sayed, A.-R., H.S. Mohran, and H.M. Abd El-Lateef, *The inhibition effect of 2, 4, 6-tris (2-pyridyl)-1, 3, 5-triazine on corrosion of tin, indium and tin–indium alloys in hydrochloric acid solution.* Corrosion science, 2010. **52**(6): p. 1976-1984.
36. Kiani, M., et al., *Inhibitory effect of some amino acids on corrosion of Pb–Ca–Sn alloy in sulfuric acid solution.* Corrosion Science, 2008. **50**(4): p. 1035-1045.
37. Şahin, M., S. Bilgic, and H. Yılmaz, *The inhibition effects of some cyclic nitrogen compounds on the corrosion of the steel in NaCl mediums.* Applied Surface Science, 2002. **195**(1-4): p. 1-7.
38. Abd El-Lateef, H.M., M.S.S. Adam, and M.M.J. Khalaf, *Synthesis of polar unique 3d metal-imine complexes of salicylidene anthranilate sodium salt. Homogeneous catalytic and corrosion inhibition performance.* Journal of the Taiwan Institute of Chemical Engineers, 2018. **88**: p. 286-304.
39. Solmaz, R., et al., *Investigation of adsorption and inhibitive effect of 2-mercaptothiazoline on corrosion of mild steel in hydrochloric acid media.* Electrochimica Acta, 2008. **53**(20): p. 5941-5952.
40. Obot, I. and N. Obi-Egbedi, *Ipomoea involcrata as an ecofriendly inhibitor for aluminium in alkaline medium.* Portugaliae Electrochimica Acta, 2009. **27**(4): p. 517-524.
41. Flis, J. and T. Zakroczymski, *Impedance study of reinforcing steel in simulated pore solution with tannin.* Journal of the Electrochemical Society, 1996. **143**(8): p. 2458.
42. Abd El-Lateef, H.M. and A.H. Tantawy, *Synthesis and evaluation of novel series of Schiff base cationic surfactants as corrosion inhibitors for carbon steel in acidic/chloride media: experimental and theoretical investigations.* RSC Advances, 2016. **6**(11): p. 8681-8700.
43. Abd El-Lateef, H.M., *Experimental and computational investigation on the corrosion inhibition characteristics of mild steel by some novel synthesized imines in hydrochloric acid solutions.* Corrosion Science, 2015. **92**: p. 104-117.
44. Mobin, M. and M.J.C.p. Rizvi, *Adsorption and corrosion inhibition behavior of hydroxyethyl cellulose and synergistic surfactants additives for carbon steel in 1 M HCl.* 2017. **156**: p. 202-214.

45. Amin, M.A. and M.M. Ibrahim, *Corrosion and corrosion control of mild steel in concentrated H2SO4 solutions by a newly synthesized glycine derivative.* Corrosion Science, 2011. **53**(3): p. 873-885.
46. Gan, W., et al., *Stable zinc anodes by in situ polymerization of conducting polymer to conformally coat zinc oxide particles.* Journal of Applied Electrochemistry, 2015. **45**: p. 913-919.
47. Abd El-Lateef, H.M. and M.A.E.A.A.A.J. Elremaily, *Divinyl sulfone cross-linked β-cyclodextrin polymer as new and effective corrosion inhibitor for Zn anode in 3.5 M KOH.* Transactions of the Indian Institute of Metals, 2016. **69**: p. 1783-1792.
48. Zeng, X., et al., *The effects of carbon coating on the electrochemical performance of Zn-Al layer double oxides in nickel-zinc secondary cells.* Ionics, 2019. **25**: p. 1223-1233.
49. Yu, Y., et al., *Al2O3 coatings on zinc for anti-corrosion in alkaline solution by electrospinning.* Coatings, 2019. **9**(11): p. 692.
50. Qu, Q., et al., *Sodium tungstate as a corrosion inhibitor of cold rolled steel in peracetic acid solution.* Corrosion science, 2009. **51**(10): p. 2423-2428.
51. Tian, B., D.B. Xie, and F.H. Wang, *Corrosion behavior of TiN and TiN/Ti composite films on Ti6Al4V alloy in Hank's solution.* Journal of applied electrochemistry, 2009. **39**: p. 447-453.
52. El-Sayed, A.-R., et al., *Effect of indium alloying with lead together with the addition of phosphoric acid in electrolyte to improve lead-acid battery performance.* Journal of Solid State Electrochemistry, 2015. **19**: p. 1463-1478.
53. Hu, J., et al., *2-Hydroxy-4-methoxy-acetophenone as an environment-friendly corrosion inhibitor for AZ91D magnesium alloy.* Corrosion Science, 2013. **74**: p. 35-43.
54. Kosari, A., et al., *Theoretical and electrochemical assessment of inhibitive behavior of some thiophenol derivatives on mild steel in HCl.* Corrosion science, 2011. **53**(10): p. 3058-3067.
55. Lee, S.-M., et al., *Improvement in self-discharge of Zn anode by applying surface modification for Zn–air batteries with high energy density.* Journal of Power Sources, 2013. **227**: p. 177-184.
56. Lee, C.W., et al., *Novel electrochemical behavior of zinc anodes in zinc/air batteries in the presence of additives.* Journal of Power Sources, 2006. **159**(2): p. 1474-1477.
57. Abd El-Lateef, H.M., et al., *Inhibition of carbon steel corrosion in CO2-saturated brine using some newly surfactants based on palm oil: experimental and theoretical investigations.* Materials Chemistry, 2013. **142**(2-3): p. 502-512.
58. Vedalakshmi, R., et al., Determination of diffusion coefficient of chloride in concrete using Warburg diffusion coefficient. Corrosion Science, 2009. 51(6): p. 1299-1307.